Protected valley states and generation of valley- and spin-polarized current in monolayer MA_2Z_4

Jiaren Yuan,[1] Qingyuan Wei,[1] Minglei Sun,[2] Xiaohong Yan,[1,*] Yongqing Cai,[3,†] Lei Shen (沈雷),[4,‡] and Udo Schwingenschlögl[2]

[1]*School of Physics and Electronic Engineering, and School of Material Science and Engineering, Jiangsu University, Zhenjiang 212013, China*

[2]*Physical Science and Engineering Division, King Abdullah University of Science and Technology, Thuwal 23955-6900, Saudi Arabia*

[3]*Joint Key Laboratory of the Ministry of Education, Institute of Applied Physics and Materials Engineering, University of Macau, Macau 999078, China*

[4]*Department of Mechanical Engineering and Engineering Science, National University of Singapore, 9 Engineering Drive 1, Singapore 117542*

(Received 15 November 2021; revised 24 April 2022; accepted 10 May 2022; published 31 May 2022)

The optical selection rules obeyed by two-dimensional materials with spin-valley coupling enable the selective excitation of carriers. We show that several members of the monolayer MA_2Z_4 (M = Mo and W; A = C, Si, and Ge; Z = N, P, and As) family are direct band-gap semiconductors with protected valley states and that circularly polarized infrared light can induce valley-selective interband transitions. Therefore, they are able to generate a close to 100% valley- and spin-polarized current under an in-plane bias and circularly polarized infrared light, which can be exploited to encode, process, and store information.

DOI: 10.1103/PhysRevB.105.195151

I. INTRODUCTION

In some two-dimensional (2D) materials, the electrons have a valley degree of freedom besides the charge and spin degrees of freedom due to the appearance of inequivalent valleys (band extrema with equal energy located at different k-points in the Brillouin zone) [1,2]. In the absence of inversion symmetry the spin-orbit coupling (SOC) can result in valley dependence of the Berry curvature, orbital magnetic moment, and optical circular dichroism [3,4]. Given the intriguing fundamental physics and potential applications in electronics and optoelectronics [5], including Hall devices [6] and photoelectric detection [7], exploring materials with a valley degree of freedom and generating valley-polarized current are important research directions.

The valley properties were investigated theoretically and experimentally for 2D materials such as graphene [8,9], SnSe [10,11], $MnPSe_3$ [12,13], and transition-metal dichalcogenides (TMDCs) [2,14]. In particular, TMDCs provide an excellent platform for the study of spin-valley coupling and valley polarization [14,15]. Different from their bulk phases, monolayer TMDCs, such as MoS_2 and $MoSe_2$, have a direct band gap with conduction band minima (CBMs) and valence band maxima (VBMs) located at both the inequivalent K- and K'-points [2]. The spin and valley degrees of freedom are coupled by the time-reversal symmetry, enabling their control [14,15]. Valley polarization can be realized by breaking the time-reversal symmetry by an external magnetic field [16], proximity effects [17], magnetic doping [18], and circularly polarized light [19,20]. For example, a large valley polarization was achieved in monolayer MoS_2 and WS_2 by circularly polarized light due to valley dependence of the optical selection rules [3,4].

The intercalated 2D semiconductor $MoSi_2N_4$ recently was synthesized by chemical vapor deposition [21]. Monolayer $MoSi_2N_4$ possesses excellent ambient stability and exhibits semiconducting behavior with high carrier mobility. Hereafter, the electronic, magnetic, transport, and optical properties of MA_2Z_4 (M = Mo and W; A = C, Si, and Ge; Z = N, P, and As) monolayers are extensively investigated. For instance, Wang *et al.* [22] predicted that MA_2Z_4 monolayer materials exhibit diverse electronic properties, including nontrivial topological properties, ferromagnetism, and superconductivity. Monolayer $MoSi_2P_4$ shows desirable transport properties that could be used for fabricating high-efficiency field-effect transistors [23,24]. Optical analysis shows that monolayer $MoSi_2N_4$ and WSi_2N_4 are promising candidates for advanced optoelectronic devices [25,26]. Furthermore, monolayer $MoSi_2N_4$, $MoSi_2P_4$, $MoSi_2As_4$, and WSi_2P_4 are predicted to be valleytronic materials with spin-valley coupling, valley-contrasting Berry curvature, and Hall effect [27–30]. Recently, it was reported that valley polarization can be induced via magnetic doping [31] and an external electric field [32]. However, a transport study on valleytronic devices is absent. It worth noting that the generation and delivery of a valley-polarized current in devices are critical for utilizing the valley degree of freedom as an information carrier for next-generation valleytronic devices [5].

Using first-principles calculations, we thus systematically investigate the 18 monolayers MA_2Z_4 (M = Mo and W; A = C, Si, and Ge; Z = N, P, and As). We obtain for six of them ($MoSi_2P_4$, $MoSi_2As_4$, WSi_2P_4, WSi_2As_4, WGe_2P_4, and WGe_2As_4) a direct band gap of 0.15 to 0.62 eV, with band extrema located at both the inequivalent K- and K'-points. All show strong spin-valley coupling. We propose a device in

*yanxh@ujs.edu.cn
†yongqingcai@um.edu.mo
‡shenlei@nus.edu.sg

which a valley- and spin-polarized current can be generated by circularly polarized light. Our results demonstrate that monolayer MA_2Z_4 offers new opportunities for valley-based electronic and optoelectronic applications.

II. METHODOLOGY

Electronic structure calculations are carried out by the Vienna Ab initio Simulation Package [33], utilizing the projector augmented wave method [34] and a cutoff energy of 450 eV. The Perdew-Burke-Ernzerhof (PBE) [35] and Heyd-Scuseria-Ernzerhof (HSE06) [36] approaches are used for the exchange-correlation functional. A $19 \times 19 \times 1$ k-grid mesh is employed. The convergence criterion of the total energy is set to 10^{-6} eV, and that of the force to 0.005 eV/Å. Spin-orbit coupling is taken into account in all calculations. The Berry curvature is calculated by the Wannier90 code [37]. The photocurrent is calculated by the Nanodcal quantum transport package [38–41] based on the Hamiltonian $H = H_{\rm el} + H_{\rm el-ph}$. The electronic contribution $H_{\rm el}$ is calculated using the first-principles and Keldysh nonequilibrium Green's function methods. The electron-photon interaction $H_{\rm el\text{-}ph}$ is calculated perturbatively using the first Born approximation $H_{\rm el-ph} = \frac{e}{m}\boldsymbol{A}\cdot\boldsymbol{p}$, where $\boldsymbol{A}$ is the electromagnetic vector potential and $\boldsymbol{p}$ is the momentum of the electron. For circularly polarized light, we have $\boldsymbol{A} = (\frac{\hbar\sqrt{\mu_r\epsilon_r}}{2N\omega\epsilon c}F_\omega)^{1/2}(\boldsymbol{e}_p b e^{-i\omega t} - \boldsymbol{e}_p^* b^\dagger e^{i\omega t})$, where ω is the frequency, F_ω is the photon flux, c is the speed of light, μ_r is the relative magnetic susceptibility, $\varepsilon_{\rm r}$ is the relative dielectric constant, ε is the dielectric constant, N is the number of photons, b and $b^\dagger$ are the annihilation and creation operators, respectively, and $\boldsymbol{e}_p = \frac{1}{\sqrt{2}}(1, \pm i, 0)$ for left-handed/right-handed circularly polarized light. The normalized (with respect to $a_0^2 eF_\omega\sqrt{\mu_r/e_r}$, where a_0 denotes the Bohr length and e is the elementary charge) current is given by $I_{\alpha,\tau,s} = \frac{e}{2\pi\hbar}\int {\rm Tr}\{i\Gamma_\alpha(E, k)[(1-f_\alpha)G_{\rm ph}^< + f_\alpha G_{\rm ph}^>]\}dE$, where $\Gamma_\alpha(E, k)$ is the line width, E is the energy, k is the wave vector, f_α is the Fermi function, α denotes the drain/source electrode, τ denotes the K/K' valley, s denotes spin up/down, and $G_{\rm ph}^</G_{\rm ph}^>$ is the greater/lesser Green's function of the electron-photon interaction.

III. RESULTS AND DISCUSSION

Figure 1 shows that monolayer MA_2Z_4 (M = Mo and W; A = C, Si, and Ge; Z = N, P, and As) has a hexagonal lattice with a D_{3h} point group (that is, without inversion symmetry) and consists of seven atomic layers of the order Z-A-Z-M-Z-A-Z. It can be regarded as a 1H-phase MZ_2 triple layer encapsulated by buckled AZ layers. The optimized lattice constants listed in Table I increase with the atomic radii of M, A, and Z.

The band structures of monolayer MA_2Z_4 are shown in Figs. 2 and 3, and the sizes and types of the band gaps are listed in Table I. The calculated band gaps of MA_2Z_4 for PBE and HSE06 in this study are in good agreement with that reported in previous literature, as listed in Table I. The results reflect rich electronic structures: MoC_2N_4, $MoSi_2N_4$, $MoGe_2N_4$, $MoGe_2P_4$, $MoGe_2As_4$, WC_2N_4, WSi_2N_4, and WGe_2N_4 are indirect band-gap semiconductors, MoC_2As_4,

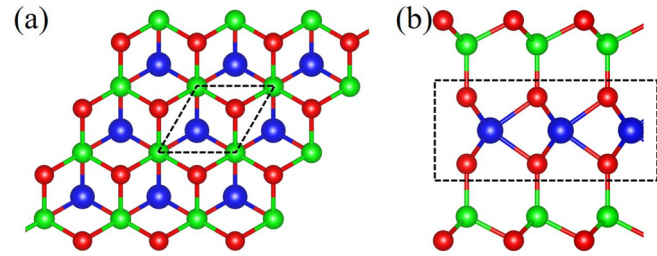

FIG. 1. (a) Top and (b) side views of the relaxed structure of MA_2Z_4. The blue, red, and green balls represent the M, A, and Z atoms, respectively. The unit cell is marked by dashed lines in (a). The structure can be regarded as an MZ_2 triple layer [resembling 1H-phase MoS_2; dashed rectangle in (b)] encapsulated by buckled AZ layers.

WC_2P_4, and WC_2As_4 are metals, and MoC_2P_4 is a direct band-gap semiconductor (better light absorption than an indirect band gap semiconductor), with the CBM and VBM located at the M-point. Most interestingly, $MoSi_2P_4$, $MoSi_2As_4$, WSi_2P_4, WSi_2As_4, WGe_2P_4, and WGe_2As_4 turn out to be direct band-gap semiconductors, with CBMs and VBMs located at both the inequivalent K- and K'-points (corners of the hexagonal Brillouin zone). Therefore, these six materials compete with the monolayer TMDCs as a platform for light-controlled valleytronics and are studied in the following in more detail.

Spin-projected (onto the z-axis) band structures are shown in Fig. 4, in which red (blue) represents the dominance of the spin-up (spin-down) component. The PBE band gap ranges from 0.15 to 0.62 eV, as listed in Table I. A comparison to HSE06 band structures, as displayed in Supplemental Material Fig. S1 [42], shows that the main band features are the same, suggesting reliability of the PBE results. In the absence of SOC, the calculated HSE06 band gap is at least 0.2 eV

TABLE I. Optimized lattice constants and PBE band gaps (HSE06 band gaps in parentheses).

		$E_{\rm gap}$ (eV)		
MA_2Z_4	a (Å)	This work	Literature	Type of band gap
MoC_2N_4	2.621	1.75		Indirect
MoC_2P_4	3.076	0.14		Direct at M
MoC_2As_4	3.257	—		—
$MoSi_2N_4$	2.911	1.78	1.74 [30,31]	Indirect
$MoSi_2P_4$	3.469	0.62 (0.86)	0.61 (0.84) [31]	Direct at K
$MoSi_2As_4$	3.617	0.51 (0.71)	0.50 (0.69) [30]	Direct at K
$MoGe_2N_4$	3.036	0.90	0.97 [21]	Indirect
$MoGe_2P_4$	3.548	0.52		Indirect
$MoGe_2As_4$	3.691	0.43		Indirect
WC_2N_4	2.638	1.66		Indirect
WC_2P_4	3.088	—		—
WC_2As_4	3.264	—		—
WSi_2N_4	2.913	2.05	2.04 [30]	Indirect
WSi_2P_4	3.475	0.29 (0.41)	0.30 [22]	Direct at K
WSi_2As_4	3.622	0.21 (0.22)		Direct at K
WGe_2N_4	3.034	1.13	1.20 [24]	Indirect
WGe_2P_4	3.552	0.23 (0.29)		Direct at K
WGe_2As_4	3.697	0.15 (0.14)		Direct at K

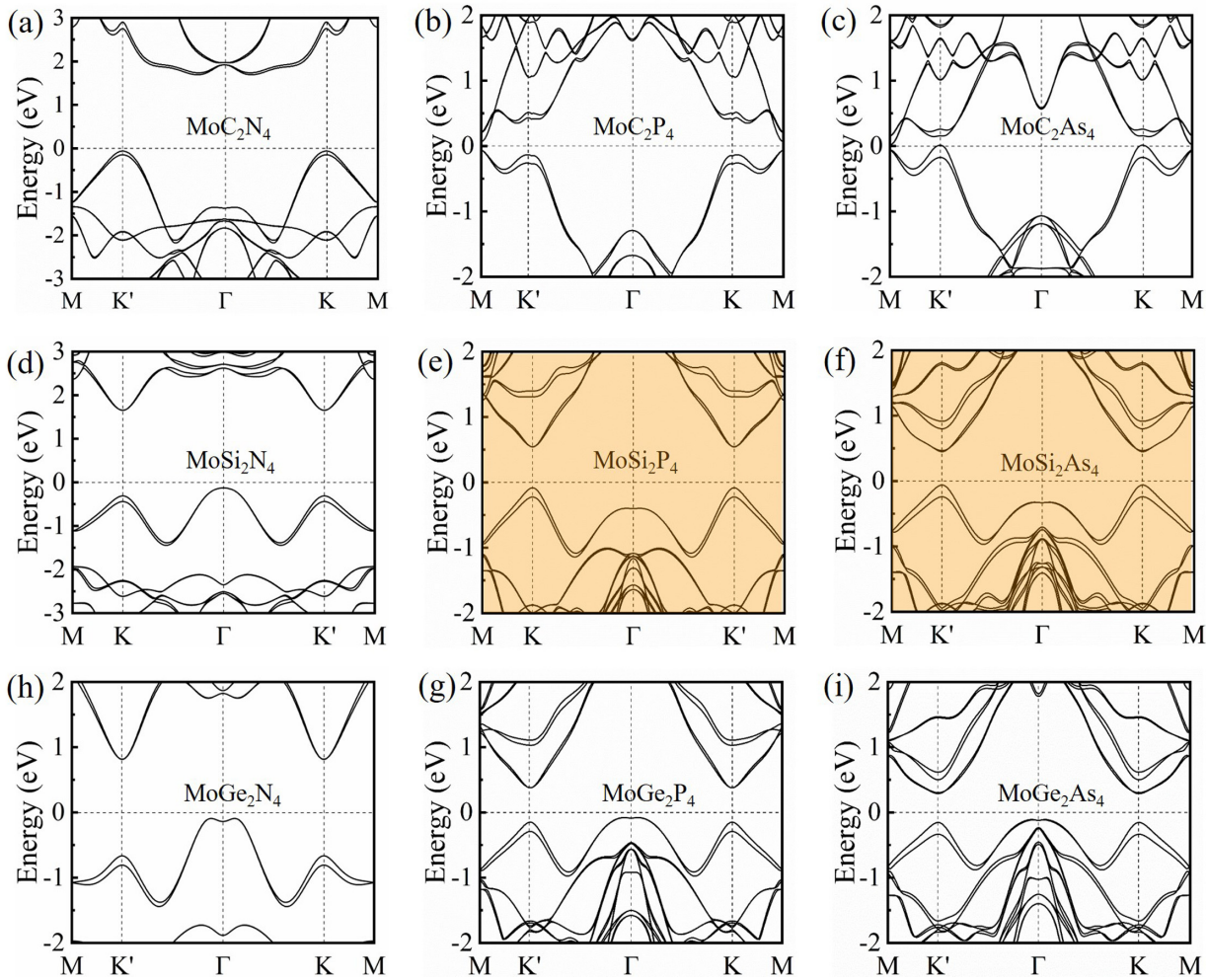

FIG. 2. (a)-(i) Band structures of monolayer MoA_2Z_4. The direct band-gap materials are shaded orange.

larger than that of PBE for all six systems. The SOC gives rise to a remarkable spin splitting near the VBM for MA_2Z_4 (139–500 meV). As a consequence, such spin splitting effectively reduces the size of the band gap. It is worth noting that the spin splittings for WSi_2As_4 and WGe_2As_4 with HSE06 ($\sim$0.7 eV) are larger than that with PBE ($\sim$0.5 eV). Thus, the final HSE06 band gaps of WSi_2As_4 and WGe_2As_4 are similar to the PBE band gaps of WSi_2As_4 and WGe_2As_4. Furthermore, the W-based compounds show larger spin splittings than the Mo-based compounds. Near the VBM, the upper (lower) band is dominated by the spin-up (spin-down) component at the K-point and the spin-down (spin-up) component at the K'-point, indicating spin-valley coupling. As the band structures in Fig. 4 are very similar, we analyze the valley properties of $MoSi_2P_4$ as a representative example.

Figure 5(a) shows schematically the valleys at the K- and K'-points. Time-reversal symmetry leads to opposite spin polarization near the VBM at the K- and K'-points. The charge densities at the VBM and CBM in Fig. 5(b) show that the valleys originate mainly from the MoP_2 layer. This conjecture is confirmed by similarity to the valleys in the band structure of 1H-phase MoP_2 (without the buckled SiP layers), as shown in Fig. 5(c). However, there are interfering states at other k-points in the energy range of the valleys in Fig. 5(c). Hence, the buckled SiP layers of $MoSi_2P_4$ not only stabilize the structure, but also protect the valley states from the interference of the P p_z and Mo $d_{3z^2-r^2}$ states (see Supplemental Material Fig. S2) [42]. The partial densities of states displayed in Fig. 5(d) demonstrate that the protected valley states are dominated by the Mo d orbitals, which split into a_1 ($d_{3z^2-r^2}$), e_1 ($d_{x^2-y^2}$, d_{xy}), and e_2 (d_{xz}, d_{yz}) groups due to the trigonal crystal field of the MoP_2 layer (see Supplemental Material Fig. S3). Specifically, the CBM is mainly due to the Mo a_1 states and the VBM is mainly due to the Mo e_1 states, as shown in the orbital-projected band structure in Fig. 5(e).

Consequently, we define the basis functions

$$|\varphi_c\rangle = \left|d_{3z^2-r^2}\right\rangle, \quad \left|\varphi_v^\tau\right\rangle = \frac{1}{\sqrt{2}}(|d_{x^2-y^2}\rangle + i\tau|d_{xy}\rangle), \tag{1}$$

where c (v) denotes the conduction (valence) band and $\tau = +1\,(-1)$ denotes the K (K') valley, to express the Hamiltonian of the two-band effective $\boldsymbol{k}\cdot\boldsymbol{p}$ model without SOC as

$$H_0^\tau = at(\tau k_x\hat{\sigma}_x + k_y\hat{\sigma}_y) + \frac{\Delta}{2}\hat{\sigma}_z, \tag{2}$$

where a denotes the lattice parameter, t denotes the effective hopping integral, $\hat{\sigma}_{x/y/z}$ denotes the Pauli matrices, and Δ denotes the band gap. Due to the common symmetry, the same

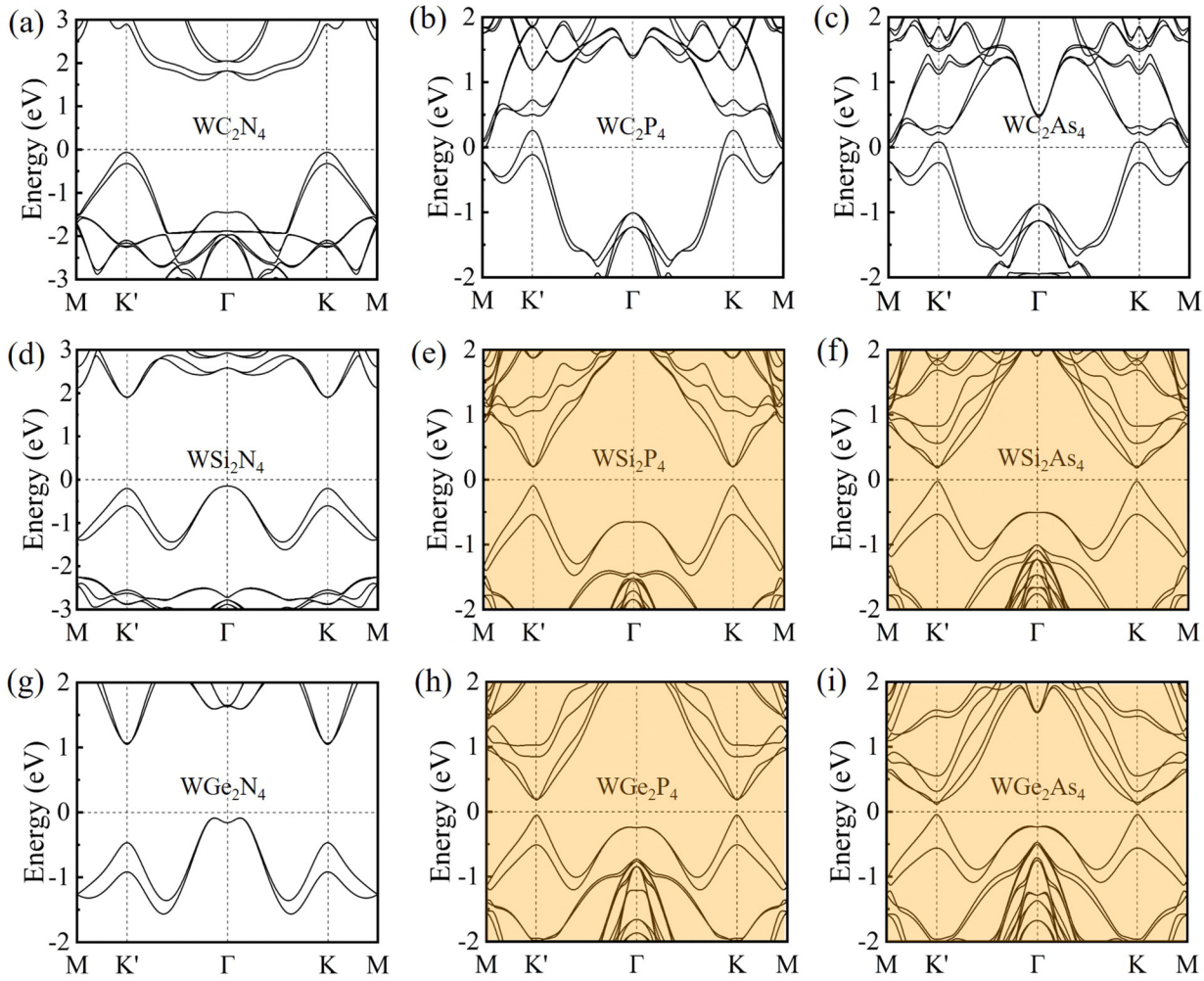

FIG. 3. (a)-(i) Band structures of monolayer WA_2X_4. The direct band gap materials are shaded orange.

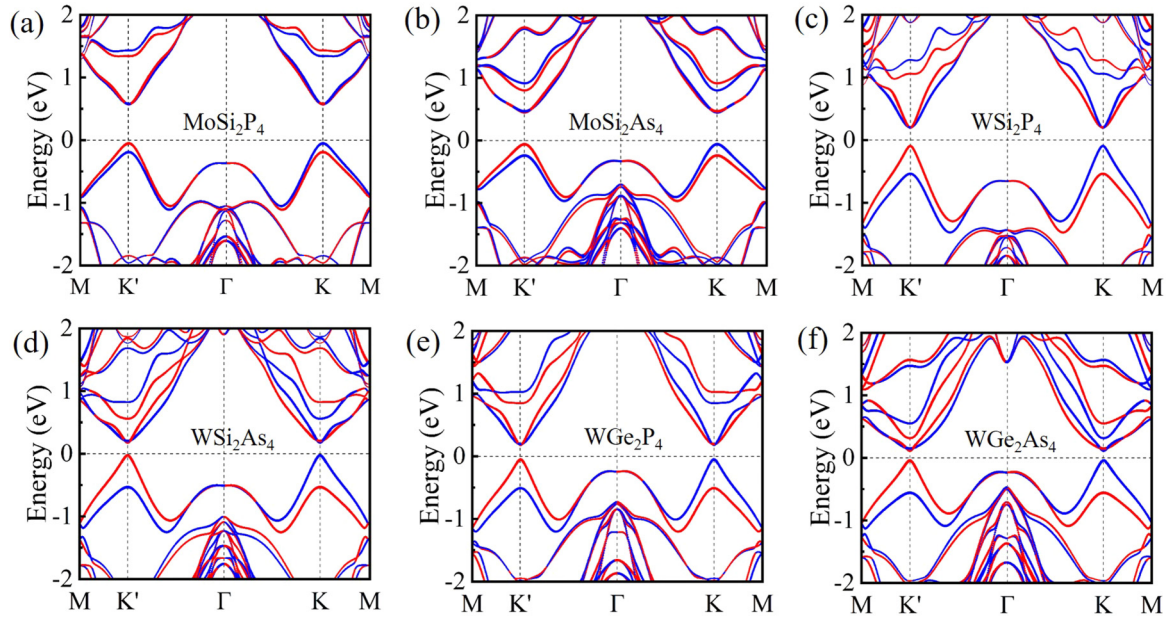

FIG. 4. Band structures of monolayer $MoSi_2P_4$, $MoSi_2As_4$, WSi_2P_4, WSi_2As_4, WGe_2P_4, and WGe_2As_4. Red (blue) represents dominance of the spin-up (spin-down) component.

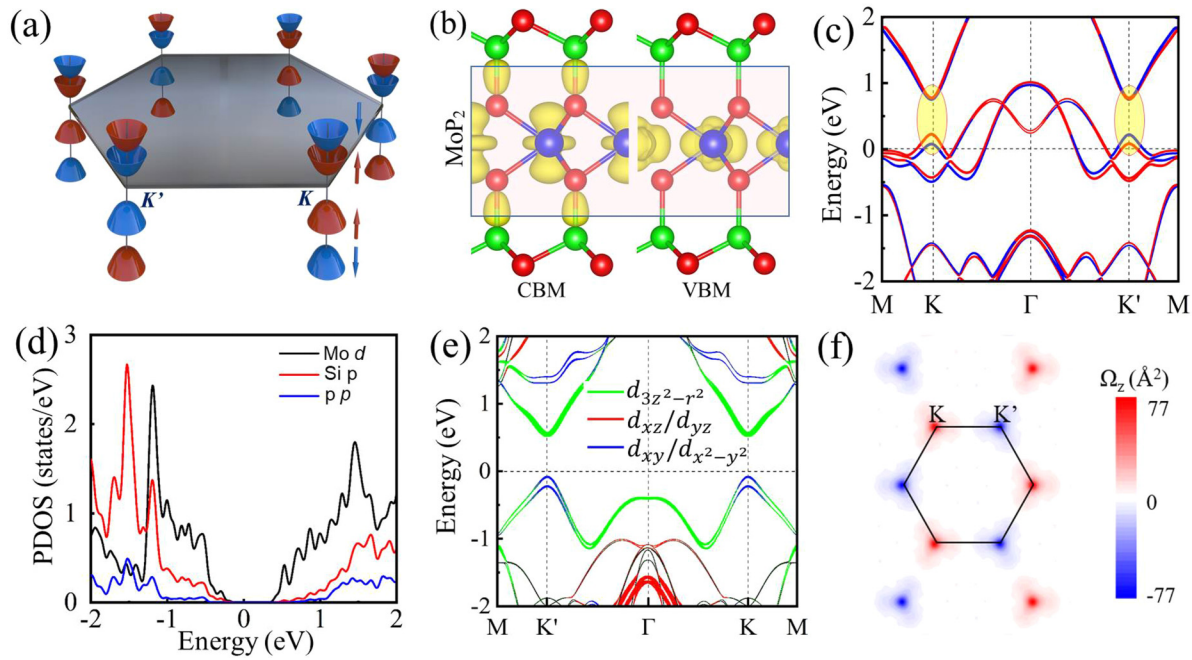

FIG. 5. (a) Schematic of the valleys near the K and K'-points, (b) charge densities at the VBM and CBM of $MoSi_2P_4$, (c) band structure of 1H-phase MoP_2, (d) partial densities of states (PDOSs) of $MoSi_2P_4$, (e) orbital-projected band structure of $MoSi_2P_4$, and (f) Berry curvature of $MoSi_2P_4$.

model applies to the 1H-phase TMDCs [2], implying that the low-energy band structures are equivalent. When the SOC is taken into account, we have

$$H_0^\tau = at(\tau k_x\hat{\sigma}_x + k_y\hat{\sigma}_y) + \frac{\Delta}{2}\hat{\sigma}_z - \lambda\tau\frac{\hat{\sigma}_z - 1}{2}\hat{s}_z, \qquad (3)$$

where 2λ is the spin splitting at the VBM (induced by the SOC) and $\hat{s}_z$ is the Pauli operator. The effective parameters of the $\boldsymbol{k}\cdot\boldsymbol{p}$ model, see Table II, are extracted from the first-principles band structures. We find that t is smaller for MoA_2Z_4 than WA_2Z_4, while Δ shows the opposite trend, with smaller values than reported for the 1H-phase TMDCs. The corresponding HSE06 values are larger but follow the same trends as the PBE values (Table II).

TABLE II. Effective hopping integral, band gap, and spin splitting extracted from the first-principles band structure.

Material	Method	t (eV Å)	Δ (eV)	2λ (eV)
$MoSi_2As_4$	PBE	2.44	0.61	0.18
	HSE06	3.18	0.86	0.24
$MoSi_2P_4$	PBE	2.36	0.70	0. 14
	HSE06	3.80	0.98	0.22
WGe_2As_4	PBE	2.84	0.45	0.50
	HSE06	3.70	0.65	0.73
WGe_2P_4	PBE	3.16	0.48	0.45
	HSE06	4.45	0.68	0.61
WSi_2As_4	PBE	3.15	0.49	0.50
	HSE06	4.18	0.70	0.70
WSi_2P_4	PBE	3.77	0.53	0.44
	HSE06	4.78	0.76	0.59

To analyze the valley properties, we evaluate the out-of-plane Berry curvature

$$\Omega_z(k) = -\sum_n\sum_{n\neq n'} f(E_n)\frac{2\mathrm{Im}\langle\psi_{nk}|v_x|\psi_{n'k}\rangle\langle\psi_{n'k}|v_y|\psi_{nk}\rangle}{(E_n - E_{n'})^2}, \qquad (4)$$

where $f(E_n)$ is the Fermi-Dirac distribution function, v_x (v_y) is the velocity operator for the x (y) direction, and ψ_{nk} is the Bloch function with eigenvalue E_n. The Berry curvature summed over 46 bands is shown in Fig. 5(f). We obtain the same absolute values but with opposite sign at the K and K' valleys. No valley-polarized current is generated under time-reversal symmetry due to equal contributions of the K and K' valleys. Application of circularly polarized light breaks the time-reversal symmetry, with the Berry curvature being proportional to the circular polarization η [43]. As the interband transitions obey different optical selection rules at the K and K' valleys, the electrons couple with left and right circularly polarized light, respectively. Thus, one can optically induce valley polarization and generate a valley-polarized current in monolayer MA_2Z_4 by excitation with circularly polarized light.

We propose a device based on monolayer MA_2Z_4 [see Fig. 6(a)] that can generate a valley-polarized current under an in-plane bias. Circularly polarized (monochromatic) light illuminates the channel between (semi-infinite) drain and source electrodes. Focusing again on $MoSi_2P_4$ as a representative example, we set the photon energy equal to the band gap, namely $\hbar\omega = 0.62$ eV, implying that only electrons located

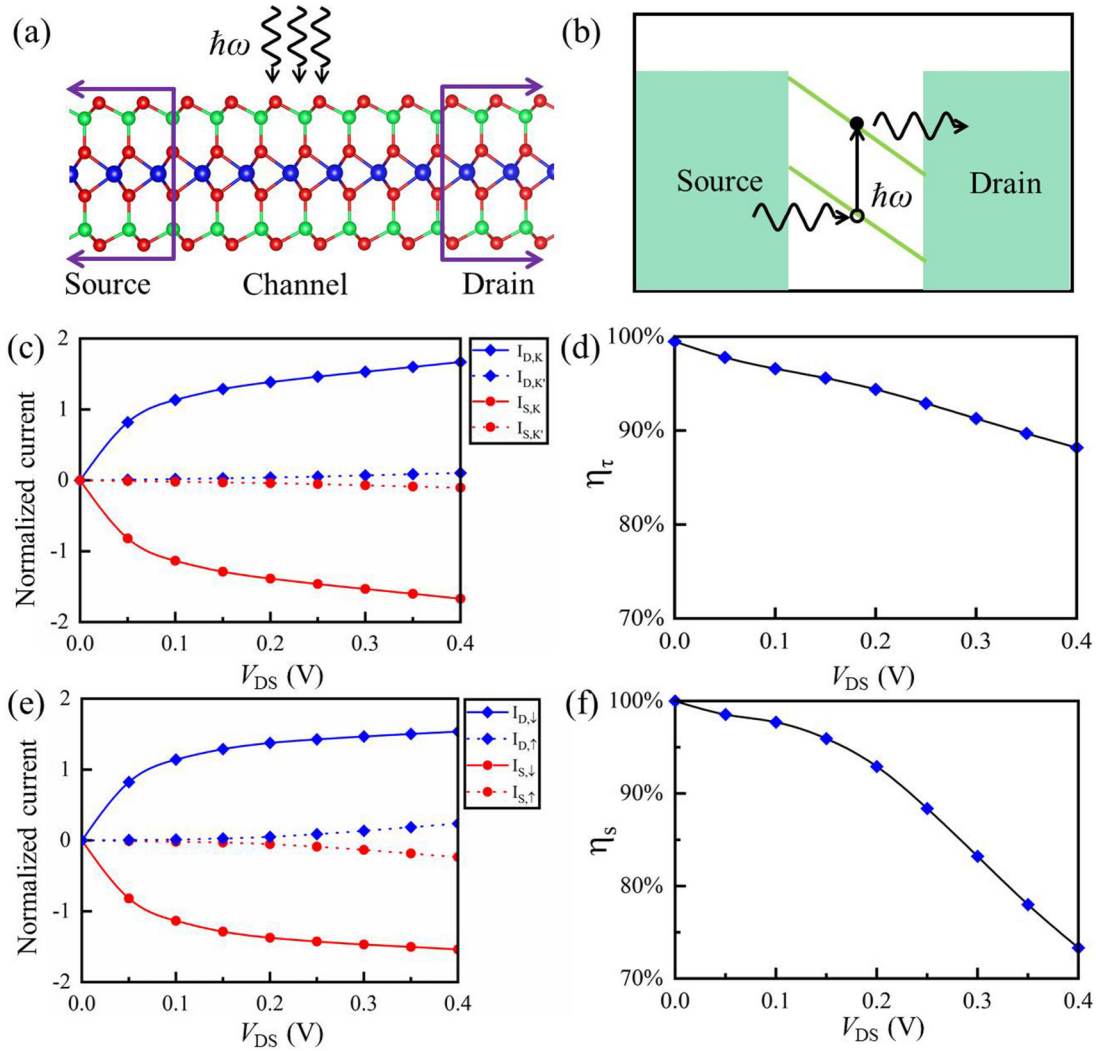

FIG. 6. (a) Schematic of the monolayer MA_2Z_4 device, (b) schematic of the generation of valley-polarized current, (c) valley components of the normalized current, (d) valley polarization, (e) spin components of the normalized current, and (f) spin polarization.

at the K- and K'-points can be excited. In the rectangular transport setup, the K- and K'-points are folded onto the points $(-1/3,\ 0,\ 0)$ and $(1/3, 0, 0)$. The drain-source voltage V_{DS} generates a valley-polarized current [see the schematic in Fig. 6(b)]. When circularly polarized light illuminates the channel and breaks the time-reversal symmetry, the electrons at the K and K' valleys absorb photons (and are excited from the VBM to the CBM) differently, which induces a population imbalance between the K and K' valleys. Under an in-plane bias, the excited electrons flow into the drain. At the same time, holes are left behind in the channel and are filled by electrons from the source, resulting in an overall current from the source to the drain.

The current generated by right-handed circularly polarized light is investigated for $V_{\mathrm{DS}} < \Delta/e$ (that is, no direct current is generated). The drain and source valley currents consist of spin-up and spin-down contributions, $I_{S/D,\tau} = I_{\mathrm{S/D},\tau,\uparrow} + I_{\mathrm{S/D},\tau,\downarrow}$. According to Fig. 6(c), the K valley currents are much larger than the K' valley currents, because the right-handed circularly polarized light excites electrons at the K valley rather than at the K' valley due to the optical selection rules. Thus, a valley-polarized current $I_{\mathrm{S/D}} = I_{\mathrm{S/D,K}} - I_{\mathrm{S/D,K}}$ is generated between the source and drain. This current is close to $I_{\mathrm{S/D},K}$, since $I_{\mathrm{S/D},K'}$ is small [see Fig. 6(d)]. Accordingly, a tremendous valley polarization $\eta_\tau = \frac{I_{\mathrm{S/D},K} - I_{\mathrm{S/D},K'}}{I_{\mathrm{S/D,K}} + I_{\mathrm{S/D},K'}}$ is achieved [see Fig. 6(d)] close to 100% at zero bias. It decreases with increasing bias, because the bias breaks the translational symmetry. However, note that this effect will decay when the channel length increases [40]. As the spin degree of freedom is locked to the valley degree of freedom (see the earlier discussion), spin currents appear simultaneously with the valley currents. Evaluation by summation over the K and K' valleys shows that the spin currents, spin-polarized current, and spin polarization follow the same trends as their valley analogues [see Figs. 6(e) and 6(f)]. A comparison of results for monolayer $MoSi_2P_4$, $MoSi_2As_4$, WSi_2P_4, WSi_2As_4, WGe_2P_4, and WGe_2As_4 at $V_{\mathrm{DS}} = 0.1$ V is given in Fig. 7, indicating that $MoSi_2P_4$, $MoSi_2As_4$, and WSi_2P_4 are most suitable for valleytronic devices, since they provide both spin and valley polarizations above 90%. Experimentally, pumping of mono-

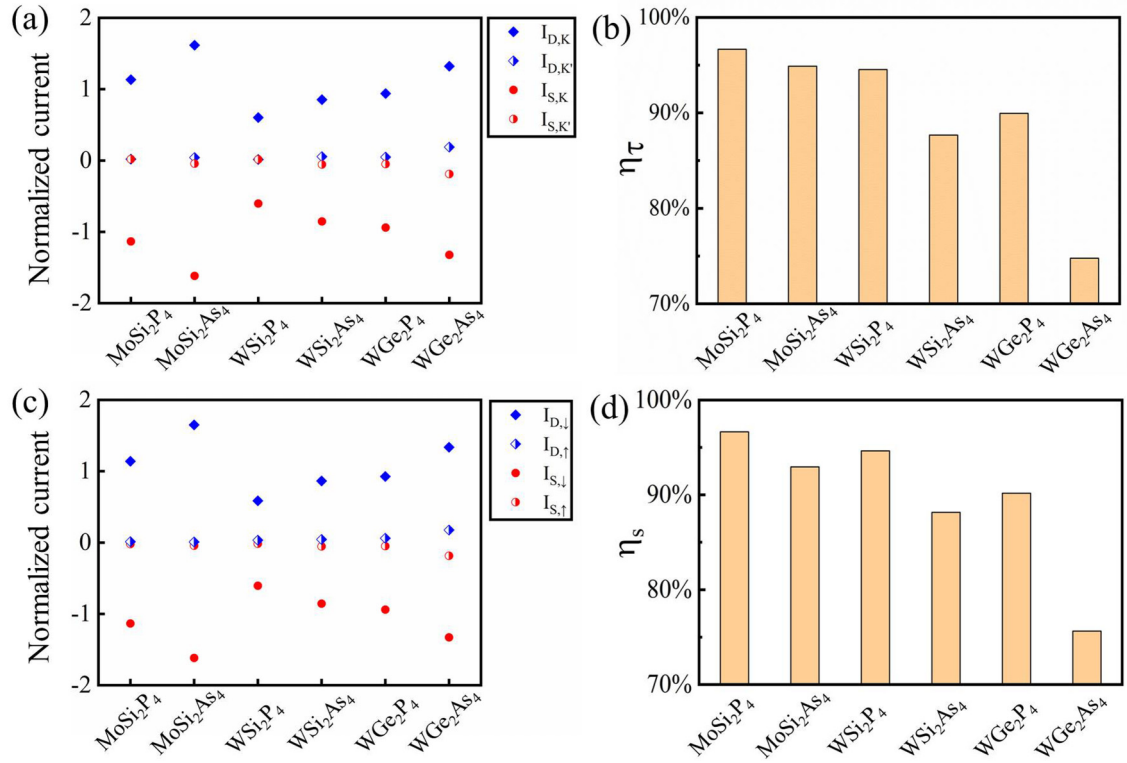

FIG. 7. (a) Valley components of the normalized current, (b) spin components of the normalized current, (c) valley polarization, and (d) spin polarization of the monolayer $MoSi_2P_4$, $MoSi_2As_4$, WSi_2P_4, WSi_2As_4, WGe_2P_4, and WGe_2As_4 devices at $V_{DS} = 0.1$ V.

layer MoS_2 with circularly polarized light can achieve a valley polarization of up to 50% [4], which is clearly surpassed by MA_2Z_4.

IV. CONCLUSION

Six members of the monolayer MA_2Z_4 ($M =$ Mo and W; $A =$ C, Si, and Ge; $Z =$ N, P, and As) family are found to be direct band-gap semiconductors, with CBMs and VBMs located at both the inequivalent K- and K'-points. These valley states originate mainly from the MZ_2 triple layer and are protected from interfering states due to the encapsulation by buckled AZ layers. Furthermore, the states near the VBM are subject to strong spin-valley coupling and significant spin splitting due to the absence of inversion symmetry and the presence of strong SOC. The direct band gap is smaller than in the case of monolayer TMDCs, falling into the infrared spectral range. Optical pumping by circularly polarized infrared light thus can induce valley polarization in monolayer MA_2Z_4 and enables the generation of a valley- and spin-polarized current under an in-plane bias. Our results demonstrate that monolayer MA_2Z_4 provides an alternative platform for investigating the interplay of the spin and valley degrees of freedom, pushing forward the development of quantum manipulation in valley-based electronic and optoelectronic devices.

ACKNOWLEDGMENTS

The authors thank Xu Gao and Mingyan Chen for providing technical support. This work was supported by the National Natural Science Foundation of China (Grants No. NSFC12004142 and No. NSFC12174158), the China Postdoctoral Science Foundation (Grant No. 2020M1350), the Natural Science Funds for Colleges and Universities in Jiangsu Province (Grant No. 20KJB140017), and the Postdoctoral Research Funding Program of Jiangsu Province (Grant No. 2020Z131). The research reported in this publication was also supported by the Singapore Ministry of Education Academic Research Fund Tier 1 (Grant No. R265-000-691-114) and funding from King Abdullah University of Science and Technology.

[1] L. Ju, L. Wang, X. Li, S. Moon, M. Ozerov, Z. G. Lu, T. Taniguchi, K. Watanabe, E. Mueller, F. Zhang, D. Smirnov, F. Rana, and P. L. McEuen, Nat. Commun. **11**, 2941 (2020).

[2] D. Xiao, G.-B. Liu, W. Feng, X. Xu, and W. Yao, Phys. Rev. Lett. **108**, 196802 (2012).

[3] H. Zeng, J. Dai, W. Yao, D. Xiao, and X. Cui, Nat. Nanotech. **7**, 490 (2012).

[4] T. Cao, G. Wang, W. P. Han, H. Q. Ye, C. R. Zhu, J. R. Shi, Q. Niu, P. H. Tan, E. Wang, B. L. Liu, and J. Feng, Nat. Commun. **3**, 887 (2012).

[5] J. R. Schaibley, H. Yu, G. Clark, P. Rivera, J. S. Ross, K. L. Seyler, W. Yao, and X. Xu, Nat. Rev. Mater. **1**, 16055 (2016).
[6] T. P. Cysne, M. Costa, L. M. Canonico, M. B. Nardelli, R. Muniz, and T. G. Rappoport, Phys. Rev. Lett. **126**, 056601 (2021).
[7] S. Y. Cha, M. J. Noh, J. Kim, J. Son, H. Bae, D. Lee, H. Kim, J. Lee, H.-S. Shin, S. W. Sim, S. Yang, S. Lee, W. Shim, C.-H. Lee, M.-H. Jo, J. S. Kim, D. Kim, and H. Choi, Nat. Nanotechnol. **13**, 910 (2018).
[8] D. Xiao, W. Yao, and Q. Niu, Phys. Rev. Lett. **99**, 236809 (2007).
[9] A. Rycerz, J. Tworzydło, and C. Beenakker, Nat. Phys. **3**, 172 (2007).
[10] K. Zhang, K. Deng, J. Li, H. Zhang, W. Yao, J. Denlinger, Y. Wu, W. Duan, and S. Zhou, Phys. Rev. Materials **2**, 054603 (2018).
[11] X.-W. Shen, W.-Y. Tong, S.-J. Gong, and C.-G. Duan, 2D Mater. **5**, 011001 (2017).
[12] Q. Pei and W. Mi, Phys. Rev. Appl. **11**, 014011 (2019).
[13] G. Long, H. Henck, M. Gibertini, D. Dumcenco, Z. Wang, T. Taniguchi, K. Watanabe, E. Giannini, and A. F. Morpurgo, ACS Nano **11**, 11330 (2017).
[14] K. F. Mak, K. He, J. Shan, and T. F. Heinz, Nat. Nanotechnol. **7**, 494 (2012).
[15] K. F. Mak, K. L. McGill, J. Park, and P. L. McEuen, Science **344**, 1489 (2014).
[16] A. Arora, R. Schmidt, R. Schneider, M. R. Molas, I. Breslavetz, M. Potemski, and R. Bratschitsch, Nano Lett. **16**, 3624 (2016).
[17] L. Xu, M. Yang, L. Shen, J. Zhou, T. Zhu, and Y. P. Feng, Phys. Rev. B **97**, 041405 (2018).
[18] Y. Cheng, Q. Zhang, and U. Schwingenschlögl, Phys. Rev. B **89**, 155429 (2014).
[19] K. L. Seyler, D. Zhong, B. Huang, X. Y. Linpeng, N. P. Wilson, T. Taniguchi, K. Watanabe, W. Yao, D. Xiao, M. A. McGuire, K.-M. C. Fu, and X. D. Xu, Nano Lett. **18**, 3823 (2018).
[20] X. Li, T. Cao, Q. Niu, J. Shi, and J. Feng, Proc. Natl. Acad. Sci. USA **110**, 3738 (2013).
[21] Y.-L. Hong, L. Wang, T. Y. Zhou, W. Ma, C. Xu, S. Feng, L. Chen, M.-L. Chen, D.-M. Sun, X.-Q. Chen, H.-M. Cheng, and W. C. Ren, Science **369**, 670 (2020).
[22] L. Wang, Y. P. Shi, M. F. Liu, A. Zhang, Y.-L. Hong, R. H. Li, Q. Gao, M. X. Chen, W. C. Ren, H.-M. Cheng, Y. Y. Li, and X.-Q. Chen, Nat. Commun. **12**, 2361 (2021).
[23] J. Huang, P. Li, X. Ren, and Z.-X. Guo, Phys. Rev. Applied **16**, 044022 (2021).
[24] H. Q. Zhao, G. F. Yang, Y. S. Liu, X. F. Yang, Y. Gu, C. L. Wei, Z. J. Xie, Q. Zhang, B. A. Bian, X. M. Zhang, X. X. Huo, and N. Y. Lu, ACS Appl. Electron. Mater. **3**, 5086 (2021).
[25] A. Bafekry, M. Faraji, D. M. Hoat, M. Shahrokhi, M. Fadlallah, F. Shojaei, S. Feghhi, M. Ghergherehchi, and D. Gogova, J Phys. D Appl. Phys. **54**, 155303 (2021).
[26] M. N. Azizabad and H. Alavi-Rad, Phys. Scripta **96**, 125826 (2021).
[27] Q. Cui, Y. Zhu, J. Liang, P. Cui, and H. Yang, Phys. Rev. B **103**, 085421 (2021).
[28] C. Yang, Z. Song, X. Sun, and J. Lu, Phys. Rev. B **103**, 035308 (2021).
[29] Y. Liu, T. Zhang, K. Dou, W. Du, R. Peng, Y. Dai, B. Huang, and Y. Ma, J. Phys. Chem. Lett. **12**, 8341 (2021).
[30] S. Li, W. Wu, X. Feng, S. Guan, W. Feng, Y. Yao, and S. A. Yang, Phys. Rev. B **102**, 235435 (2020).
[31] H. Ai, D. Liu, J. Geng, S. Wang, K. H. Lo, and H. Pan, Phys. Chem. Chem. Phys. **23**, 3144 (2021).
[32] R. Islam, B. Ghosh, C. Autieri, S. Chowdhury, A. Bansil, A. Agarwal, and B. Singh, Phys. Rev. B **104**, L201112 (2021).
[33] G. Kresse and J. Furthmüller, Comp. Mater. Sci. **6**, 15 (1996).
[34] G. Kresse and J. Furthmüller, Phys. Rev. B **54**, 11169 (1996).
[35] J. P. Perdew, K. Burke, and M. Ernzerhof, Phys. Rev. Lett. **77**, 3865 (1996).
[36] J. Heyd and G. E. Scuseria, J. Chem. Phys. **121**, 1187 (2004).
[37] A. A. Mostofi, J. R. Yates, G. Pizzi, Y.-S. Lee, I. Souza, D. Vanderbilt, and N. Marzari, Comput. Phys. Commun. **185**, 2309 (2014).
[38] J. Taylor, H. Guo, and J. Wang, Phys. Rev. B **63**, 245407 (2001).
[39] D. Waldron, P. Haney, B. Larade, A. MacDonald, and H. Guo, Phys. Rev. Lett. **96**, 166804 (2006).
[40] L. Zhang, K. Gong, J. Chen, L. Liu, Y. Zhu, D. Xiao, and H. Guo, Phys. Rev. B **90**, 195428 (2014).
[41] Y. Xie, L. Zhang, Y. Zhu, L. Liu, and H. Guo, Nanotechnology **26**, 455202 (2015).
[42] See Supplemental Material at http://link.aps.org/supplemental/10.1103/PhysRevB.105.195151 for HSE06 band structures for six direct band gap materials, projected band structures of MoP_2 and partial densities of states of monolayer $MoSi_2P_4$.
[43] Y. Liu, S. A. Yang, and F. Zhang, Phys. Rev. B **97**, 035153 (2018).